On the continuous mechanics first- and second-order formulations for non-equilibrium nucleation: Derivation and applications

I. L. Ferreira (✉ ileao@ufpa.br)

Federal University of Pará, UFPA

A. L. S. Moreira

Federal University of Pará, UFPA

Additional Declarations: No competing interests reported.

On the continuous mechanics first- and second-order formulations for non-equilibrium nucleation: Derivation and applications

I.L. Ferreira[1,a*], A.L.S. Moreira[1,b]

[1]*Faculty of Mechanical Engineering, Federal University of Pará, UFPA, Augusto Corrêa Avenue 1,*
66075-110, Belém, PA, Brazil
[a*]ileao@ufpa.br, [b]alsm@ufpa.br
*Corresponding author

Abstract

Nucleation and growth are phenomena that can be applied to several fields of science and technology. On the other hand, nucleation depends on the cooling rate, dislocating the equilibrium, as surface energy depends on the created and deformed surface area. The crystalline/glassy transition limit dependence on the thermal gradient is also analyzed. In this paper, under continuum mechanics, first- and second-order nonequilibrium nucleation formulation models are derived, and a phase-change moving interface is considered in the thermal field. Important nucleation variables are plotted against the cooling rate for several nucleation angles. It is coupled with a theoretical model for the molar-specific heat capacity of solids to analyse its dependence on nucleation kinetics.

Keywords: Nonequilibrium phase change; Phase nucleation; First- and second-order formulations; Nonequilibrium nucleation.

1 Introduction

The study of the nucleation process is of paramount importance because it is related to many areas of scientific and technological interest, such as weather forecasting and climate studies, concerning the key factors responsible for climate change, volcanology, and mineral crystallization, among other geophysical and astrogeophysical applications. In the materials, mechanics, electronics, aerospace, and pharmaceutical industries, the latter highlights the synthesis of proteins for the most diverse medical treatments. Nucleation can be defined as the formation of one new phase with high free energy to an organized structure or pattern with a low free energy in specific positions and characterized by well-defined contours that separate

the medium that created it [1,2]. Nucleation is a general-purpose phenomenon with applicability in many processes, such as crystallization, melting, boiling, condensation, glass transition [3], and recently in rapid prototyping additive manufacturing [4,5]. Phase nucleation is complex and unfinished matter that requires permanent efforts in several fields, from analyses of formulations based on classical thermodynamics for continuous media and statistical thermodynamics for noncontinuous media using MD molecular dynamics to quantum theory, which underlies ab initio methods. The scale of the problem dictates the type of theory best suited. At large spatial and temporal scales, when possible to employ, theory based on continuum mechanics is more appropriate since it can handle problems such as weather forecasting and geophysical and manufacturing processes within adequate spatial and temporal scalability. However, MD molecular dynamics based on classical physics and ab initio methods based on quantum mechanics would require unimaginable computing power and considerably long response times from the currently available computing capabilities, being suitable only for systems with tens, hundreds to a few thousand atoms. Classical nucleation theory, known as CNT, has its origins in Fahrenheit's work on the supercooling of water, later receiving thermodynamic support in studies of droplet formation on a supersaturated vapor. Volmer and Weber, among others, formulated the kinetics of vapor condensation, later extended by Turnbull and Fisher to the case of nucleation of condensed phases [6]. The basic mechanism underpinning CNT consists of a change in the free energy of the system during homogeneous nucleation of a spherical nucleus. The important variables are the cluster volume of the radius, the volume of a single molecule, the supersaturation ratio and the specific surface energy of the interface between the drop and the surroundings. The free energy is based on a positive contribution of surface energy and a negative contribution of bulk energy presenting a maximum, providing the critical radius, beyond which the system energy begins to decrease. Polymorphism is not considered by CNT, and it also cannot explain the vanishing nucleation

barrier at high supersaturation [1,6]. It fails in predicting vapor-liquid systems, and it was found to disagree by a factor of 2000 [7]. Furthermore, CNTs do not properly account for dipole-dipole interactions in the case of polar vapors. Experimental evidence of nucleation in crystallizing solutions has shown that the formation of a cluster with a higher density and its structural reorganization to form a crystal are separated in the time zone, which requires at least two order parameters [7]. Density functional theory (DFT) is a nonclassical nucleation theory that can be applied to several nucleation phenomena, such as vapor-liquid and liquid-solid phenomena, in addition to explaining spinodal decomposition. DFT is based on a density function approach concerning the intrinsic free energy of the system and the molecular number density [8,9]. To apply this theory, knowledge of the intermolecular potentials of the system is needed, which are approximated from hard-sphere perturbation theory. This requires molecular potentials that are not available for complex compounds. Another approach is the diffuse interface theory (DIT), which considers a strong dependence of the surface tension on the curvature in an attempt to correct the assumption of a sharp interface of the classical droplet model by considering the bulk solid and liquid enthalpies and entropies inside the interface domain [10,11]. The DIF theory succeeds in predicting a wide range of substances, including hydrocarbon liquids, liquid metals and oxide glasses. However, the growing experimental evidence of nucleation events in crystallizing solutions has shown that the formation of clusters with a higher density and their structural reorganization to form a crystal are separated in the time zone, which requires at least two order parameters, density and structure, to differentiate old and new phases. This has led to the evolution of the concept of a nonclassical two-step pathway to nucleation, which is discussed in the next section. Experimental evidence of the nucleation process points to the prior formation of clusters of atoms in the liquid with structural reorganization that will form the new crystalline phase that is separated into time zones that require two or more order parameters that differentiate the initial phase from the final phase.

These observations have led to so-called nonclassical nucleation path models [12-17]. This evidence agrees with what has been recently observed by Ferreira and coworkers [18,19] and with this work that presents the derivation of a set of equations based on continuum mechanics for coupling with the surface-stress tensor and with the First and Second Laws of Thermodynamics for homogeneous and heterogeneous nonequilibrium nucleation. Authors have found that there cannot be nucleation of a phase whose supercooling is zero, as it would cause the surface entropy to rise to levels that would not permit any crystal ordering, characterized by the bulk entropy [20]. This implies that for heterogeneous non-equilibrium nucleation, different-ordered liquid structure atoms organized in short-range clusters with properties similar to the original liquid act as a substrate.

2 Mathematical Formulation of Nucleation

The nucleation of phases is very complex in nature because it is dependent on the local thermal gradient $\nabla\mathbf{T}$, as has been demonstrated recently by Ferreira [18] and Ferreira et al. [19]. By considering a continuum medium, the thermal gradient can be expressed in terms of thermodynamic variable gradients of work ($\boldsymbol{\sigma}V$ surface tension or $-\boldsymbol{P}V$ pressure for inviscid flow and volume), composition, and temperature throughout the Gibbs-Thomson-Ferreira equation (GTF equation), which directly measures the level of structural ordering of a new formed phase from another primary phase at a given thermal gradient level. While these authors were working on the prediction of secondary arm-spacing as a function of cooling rate (120 to 1560 $K.min^{-1}$) and the local solidification time for multicomponent alloys considering several aluminum-based alloy systems they observed that the both surface energy and Gibbs Thompson coefficient are dependent on the cooling rate as well as composition, temperature and pressure gradients, i.e., the thermal field gradient $\nabla\mathbf{T}$. Thus, the Gibbs-Thomson coefficient was derived

as $\Gamma^{Al} = f\left(\nabla\tilde{T}, \nabla C^{Cu}, \nabla C^{Si}, \nabla C^{Mg}, \nabla C^{Si}\right)$ [18], later generalized in terms of thermal field gradient $\nabla\mathbf{T}$ as $\Gamma^{Al} = f\left(\nabla P, \nabla V, \nabla C^i, \nabla\tilde{T}\right)$ [19-21] according to Eq. (1),

$$\Gamma(\vec{r}) = \nabla\mathbf{T} \cdot \hat{n}\, A(\vec{r}) = \left[\frac{\partial T}{\partial \boldsymbol{E}} \cdot \nabla \boldsymbol{E}\right] \cdot \hat{n}\, A(\vec{r}) \tag{1}$$

where $\boldsymbol{E}$ denotes the total energy of the system, $\nabla\mathbf{T}$ is the normal thermal gradient to a created and deformed surface area $A(\vec{r})$ which can be expressed as $\nabla\mathbf{T} = \left[\frac{\partial T}{\partial \boldsymbol{\sigma}V} \cdot \nabla\boldsymbol{\sigma}V + \sum_{i=1}^{n-1}\frac{\partial T}{\partial C_i} \cdot \nabla C_i + \nabla T\right] \cdot \hat{n}\, A(\vec{r})$, as a function of work $\nabla\boldsymbol{\sigma}V$, concentration ∇C_i, and temperature ∇T gradients. By considering no viscous effects, the thermodynamic pressure is giving by $\boldsymbol{\sigma} = -\boldsymbol{p}$, for incompressible flow $\nabla\vec{V} = 0$ and inviscid flow $2\mu\frac{\partial u_i}{\partial x_i} = 0$ according to Eq. (2),

$$\sigma_{ii} = -p_{ii} - \frac{2}{3}\mu_{ii}\,\nabla\vec{V} + 2\mu_{ii}\frac{\partial u_i}{\partial x_i}. \tag{2}$$

where, σ_{ii} and μ_{ii} are the fluid surface tension and viscosity, respectively. Furthermore, σ_{ii} is a fluid property and σ_{SL} is a consequence of the new created and deformed surface area $A(\vec{r})$ as result of surface stress-tensor solution [19].

Surface tension and viscosity vary with both temperature and solute concentration. There are countless possibilities to get around this problem, for instance, solving accordingly the intermolecular potentials for these properties or using excess relationships in the realms of computational thermodynamics. An interesting alternative solution for the fluid surface tension σ_{ii} and viscosity μ_{ii} in terms of temperature and concentration was recently proposed by Ferreira et al. [22,23] and Kaptay [24], respectively. For the case of surface tension of multicomponent alloys based on the surface tension–viscosity relationship, similarly to the Egry's approach [25] for pure component fluids which is associated with the Seetharaman–Du Sichen equation [26] for the calculation of Gibbs energy of activation of viscous flow ΔG^*

(Seetharaman–Du Sichen -SDS) as well as the viscosity equation for multicomponent fluid

proposed by Kaptay [24] which can be applied to any liquid or gas providing,

$$\sigma_{ii}(T, x_1, x_2, \dots, x_n) = \frac{15}{16} \frac{h \cdot N_{Av}}{\sum_{i=1}^{n} x_i \cdot V_i + \Delta V^E} \cdot \sqrt{\frac{\bar{R} \cdot T}{\sum_{i=1}^{n} x_i \cdot M_i}} \cdot \exp\left[\frac{\Delta G^* - \alpha \cdot \Delta H}{\bar{R} \cdot T}\right] \tag{3}$$

According Kaptay [24], the viscosity can be expressed in terms of temperature and

composition as follows,

$$\eta_{ii}(T, x_{Al}, x_{Si}, x_{Cu}, x_{Mg}) = \frac{h \cdot N_{Av}}{\sum_{i=1}^{n} x_i \cdot V_i + \Delta V^E} \exp\left[\frac{\Delta G^* - \alpha \cdot \Delta H}{\bar{R} \cdot T}\right] \tag{4}$$

The analysis was performed by comparing a modified version of Rappaz and Böettinger's

[27,28] secondary arm spacing model derived by Ferreira et al. [21] with experimental data.

The surface area $A(\vec{r})$ depends on the geometry of the nucleating phase as a consequence of

thermodynamic variables such as work $\boldsymbol{\sigma}V$ (pressure, surface tension and volume),

composition, temperature, as seen from the pressure vs. temperature phase diagrams obtained

from first-principles calculations found in Kapil et al. [29] and from the experimental study on

the ice crystal formation [30]. The initially derived model by Ferreira [18] could not predict

either the decrease in crystal regularity or the crystalline-glassy transition associated with the

cooling rate and composition [31,32]. Ferreira et al. [19,20], by considering the volumetric and

surface entropy relationship, added both effects to the formulation of nucleation,

$$\Gamma(\vec{r}) = \frac{\gamma_{SL}}{\Delta S - \frac{1}{\Delta T} \frac{\partial \gamma_{SL}}{\partial \vec{r}}\Big|_{\vec{r} = \vec{r}_C}} = \nabla\mathbf{T} \cdot \hat{n} \, A(\vec{r}) = \left[\frac{\partial T}{\partial \boldsymbol{\sigma}V} \cdot \nabla\boldsymbol{\sigma}V + \sum_{i=1}^{n-1} \frac{\partial T}{\partial C_i} \cdot \nabla C_i + \nabla T\right] \cdot \hat{n} \, A(\vec{r})$$

$$\tag{5}$$

The authors derived relationships for nonequilibrium critical free energy and nucleation

rate considering homogeneous and heterogeneous nucleation. By carrying out detailed analysis

on the obtained equations and experimental data, a drift in the nucleation angle in relation to

the nucleation radius as a function of the cooling rate was noted, which could not be explained

by Eq. (2). To conform the numerical analysis, a new derivation of the non-equilibrium

nucleation considering first- and second-order formulations was more recently conducted by Ferreira and Moreira [20], which will be expanded and further analysed in the present work. Both energy balances are considered for the initial nucleus to be homogeneous spherical and heterogeneous spherical cap nucleation. After further development of the moving interface between phases, it can develop into other more favorable geometric shapes to fit the thermodynamic conditions imposed by the thermal gradient, which can quickly evolve into a sphere of variable radius [18-20] to fit a more suitable geometric shape for a suitable nucleating/coalescent moving transformation interface.

$$\Delta G_{\text{Het}} = (2 - 3\cos\theta + \cos^3\theta)\left(-\frac{1}{3}\pi\, r^3\, \Delta S_V\, \Delta T + \pi\, r^2\, \gamma_{SL}\right) = \left(-\frac{1}{3}\pi\, r^3\, \Delta S_V\, \Delta T + \pi\, r^2\, \gamma_{SL}\right) f(\theta) \qquad (6)$$

and,

$$\Delta G_{Hom} = -\frac{4}{3}\pi\, r^3 \Delta S_V\, \Delta T + 4\,\pi\, r^2\, \gamma_{SL} \qquad (7)$$

In the case of heterogeneous nucleation, the missing nucleation angle drift in Eq. (5) can be found by deriving Eq. (6). Here, both derivations for heterogeneous and homogeneous nucleation will be presented. Nevertheless, the focus will remain on heterogeneous nucleation. The analytical derivation in relation to the critical nucleation radius provides quadratic relationships for heterogeneous and homogeneous nucleation as follows:

$$-\left[\left(\frac{\partial \Delta S_V}{\partial r}\Delta T + \Delta S_V\frac{\partial \Delta T}{\partial r}\right)f(\theta) + \Delta S_V\,\Delta T\frac{\partial f(\theta)}{\partial r}\right]r_C^2 - 3\left[\left(\Delta S_V\,\Delta T - \frac{\partial \gamma_{SL}}{\partial r}\right)f(\theta) - \gamma_{SL}\frac{\partial f(\theta)}{\partial r}\right]r_C + 6\gamma_{SL} = 0 \qquad (8)$$

and, for homogeneous nucleation

$$-\left(\frac{\partial \Delta S_V}{\partial r}\Delta T + \Delta S_V\frac{\partial \Delta T}{\partial r}\right)r_C^2 - 3\left(\Delta S_V\,\Delta T - \frac{\partial \gamma_{SL}}{\partial r}\right)r_C + 6\,\gamma_{SL} = 0 \qquad (9)$$

The resulting Eq. (8) and Eq. (9) are both quadratic functions, demanding a second-order critical nucleation radius analysis to be carried out. A second-order formulation model for the

nonequilibrium nucleation can be derived by solving r_c for Eq. (8) and Eq. (9), the following equation is obtained:

$r_{C,Het}$

$$= \frac{3\left[\left(\Delta S_V \, \Delta T - \frac{\partial \gamma_{SL}}{\partial r}\right)f(\theta) - \gamma_{SL}\frac{\partial f(\theta)}{\partial r}\right] \pm \sqrt{9\left[\left(\Delta S_V \, \Delta T - \frac{\partial \gamma_{SL}}{\partial r}\right)f(\theta) - \gamma_{SL}\frac{\partial f(\theta)}{\partial r}\right]^2 + 24\left[\left(\frac{\partial \Delta S_V}{\partial r}\Delta T + \Delta S_V\frac{\partial \Delta T}{\partial r}\right)f(\theta) + \Delta S_V \, \Delta T\frac{\partial f(\theta)}{\partial r}\right]\gamma_{SL}}}{-2\left[\left(\frac{\partial \Delta S_V}{\partial r}\Delta T + \Delta S_V\frac{\partial \Delta T}{\partial r}\right)f(\theta) + \Delta S_V \, \Delta T\frac{\partial f(\theta)}{\partial r}\right]}$$

$$= \frac{2 \, \Gamma_{Het}}{\Delta T} = \frac{2}{\Delta T} \, \nabla \boldsymbol{T} \cdot \hat{n} \, A(\vec{r})$$

(10)

and, for homogeneous nucleation

$$r_{C,Hom} = \frac{3\left(\Delta S_V \, \Delta T - \frac{\partial \gamma_{SL}}{\partial r}\right) \pm \sqrt{9\left(\Delta S_V \, \Delta T - \frac{\partial \gamma_{SL}}{\partial r}\right)^2 + 24\left(\frac{\partial \Delta S_V}{\partial r}\Delta T + \Delta S_V\frac{\partial \Delta T}{\partial r}\right)\gamma_{SL}}}{-2\left(\frac{\partial \Delta S_V}{\partial r}\Delta T + \Delta S_V\frac{\partial \Delta T}{\partial r}\right)} = \frac{2 \, \Gamma_{Hom}}{\Delta T} = \frac{2}{\Delta T} \, \nabla \boldsymbol{T} \cdot \hat{n} \, A(\vec{r})$$

(11)

Let us analyze the second-order solution for the critical radius r_c for both cases:

i. The Glassy-Crystalline Transition is easily derived by making $3\left[\left(\Delta S_V \, \Delta T - \frac{\partial \gamma_{SL}}{\partial r}\right)f(\theta) - \gamma_{SL}\frac{\partial f(\theta)}{\partial r}\right] = 0$ in Eq. (8) and similar to Eq. (9):

- For heterogeneous nucleation

$$3\left[\left(\Delta S_V \, \Delta T - \frac{\partial \gamma_{SL}}{\partial r}\right)f(\theta) - \gamma_{SL}\frac{\partial f(\theta)}{\partial r}\right] = 0$$

(12a)

$$\left(\Delta S_V \, \Delta T - \frac{\partial \gamma_{SL}}{\partial r}\right)\frac{1}{\gamma_{SL}} = \frac{1}{f(\theta)}\frac{\partial f(\theta)}{\partial r}$$

(12b)

$$r_{C,Het} = \sqrt{\frac{6 \, \gamma_{SL}}{\left[\left(\frac{\partial \Delta S_V}{\partial r}\Delta T + \Delta S_V\frac{\partial \Delta T}{\partial r}\right)f(\theta) + \Delta S_V \, \Delta T\frac{\partial f(\theta)}{\partial r}\right]}} = \frac{2 \, \Gamma_{Het}}{\Delta T} = \frac{2}{\Delta T} \, \nabla \boldsymbol{T} \cdot \hat{n} \, A(\vec{r})$$

(12c)

- For homogeneous nucleation

$$3\left(\Delta S_V \, \Delta T - \frac{\partial \gamma_{SL}}{\partial r}\right) = 0$$

(13a)

$$\frac{\partial \gamma_{SL}}{\partial r} = \Delta S_V \, \Delta T$$

(13b)

$$r_{C,Hom} = \sqrt{\frac{6 \, \gamma_{SL}}{\left(\frac{\partial \Delta S_V}{\partial r}\Delta T + \Delta S_V\frac{\partial \Delta T}{\partial r}\right)}} = \frac{2 \, \Gamma_{Hom}}{\Delta T} = \frac{2}{\Delta T} \, \nabla \boldsymbol{T} \cdot \hat{n} \, A(\vec{r})$$

(13c)

ii. The second-order analysis of the maximum critical radius r_{Cmax} arising from the correlation between the bulk and surface free energies Eq. (6) and Eq. (7), providing a maximum beyond which the system energy begins to decrease:

- For heterogeneous nucleation

$$r_{Cmax,Het} = \frac{3\left[\left(\Delta S_V \, \Delta T - \frac{\partial \gamma_{SL}}{\partial r}\right)f(\theta) - \gamma_{SL}\frac{\partial f(\theta)}{\partial r}\right]}{-2\left[\left(\frac{\partial \Delta S_V}{\partial r}\Delta T + \Delta S_V \frac{\partial \Delta T}{\partial r}\right)f(\theta) + \Delta S_V \, \Delta T \frac{\partial f(\theta)}{\partial r}\right]} \qquad (14)$$

- For homogeneous nucleation

$$r_{Cmax,Hom} = \frac{3\left(\Delta S_V \, \Delta T - \frac{\partial \gamma_{SL}}{\partial r}\right)}{-2\left(\frac{\partial \Delta S_V}{\partial r}\Delta T + \Delta S_V \frac{\partial \Delta T}{\partial r}\right)} \qquad (15)$$

iii. Analysis of the first-order nonequilibrium nucleation formulation is useful in many applications and can be obtained by making $r_C^2 \sim 0$ in Eq. (8) and Eq. (9):

- For heterogeneous nucleation

$$r_{C,Het} = \frac{2\,\gamma_{SL}}{\Delta T\left[\left(\Delta S_V - \frac{1}{\Delta T}\frac{\partial \gamma_{SL}}{\partial r}\right)f(\theta) - \frac{\gamma_{SL}}{\Delta T}\frac{\partial f(\theta)}{\partial r}\right]} = \frac{2\,\Gamma_{Het}}{\Delta T} \qquad (16a)$$

$$\Gamma_{Het} = \frac{\gamma_{SL}}{\left(\Delta S_V - \frac{1}{\Delta T}\frac{\partial \gamma_{SL}}{\partial r}\right)f(\theta) - \frac{\gamma_{SL}}{\Delta T}\frac{\partial f(\theta)}{\partial r}} \qquad (16b)$$

- For homogeneous nucleation

$$r_{C,Hom} = \frac{2\,\gamma_{SL}}{\Delta T\left(\Delta S_V - \frac{1}{\Delta T}\frac{\partial \gamma_{SL}}{\partial r}\right)} = \frac{2\,\Gamma_{Hom}}{\Delta T} \qquad (17a)$$

$$\Gamma_{Hom} = \frac{\gamma_{SL}}{\left(\Delta S_V - \frac{1}{\Delta T}\frac{\partial \gamma_{SL}}{\partial r}\right)} \qquad (17b)$$

3. Application of GTF for Nucleating/Coalescent Moving Interface

The evolution of a transformation interface from nucleation can only be explained by considering a relationship between the heat flow associated with the thermal field due to successive nucleation and coalescing processes of the interface that moves between two successive nucleation positions. Fig. (1) shows three nucleation positions associated with the critical radius as a function of cooling rate for the thermal field in the vicinity of the liquidus isotherm. The effect of cooling rates on the nucleation process as observed in recent works [19-

20]. For certain combinations of the compositional ∇C_i, viscous work $\nabla \boldsymbol{\sigma} V$ or thermodynamic pressure $-\nabla \mathbf{P} V$ in absence of viscous effect, and temperature $\nabla \tilde{T}$ gradients that make up the thermal gradient, there will exist values for which nucleation will not occur, in which case it is represented by a curve where the temperature continuously decreases.
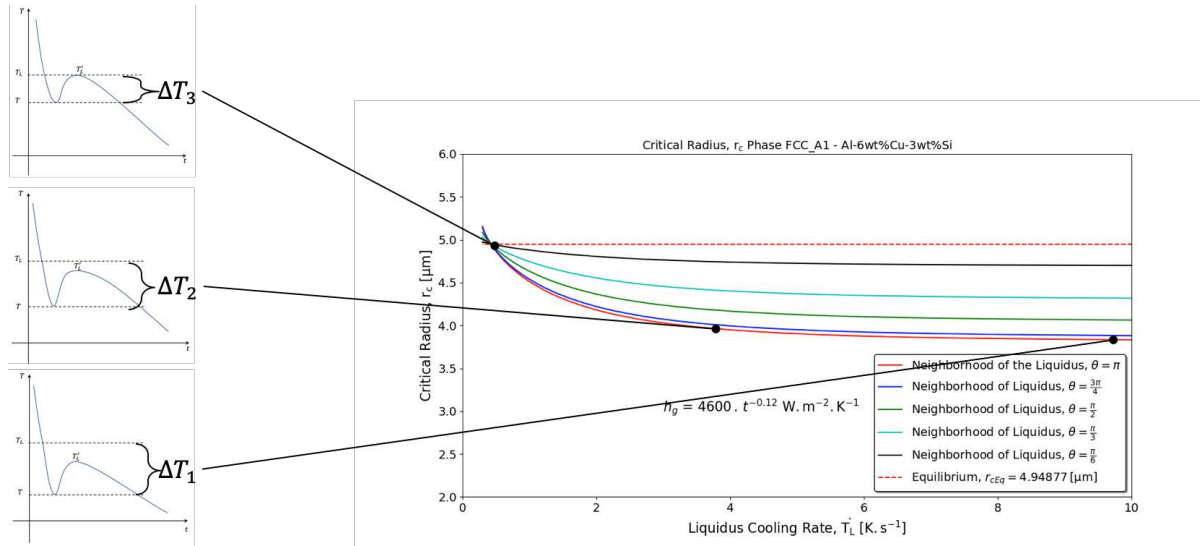

Fig. 1 Nucleation conditions at critical radii expressed as a function of the cooling rate in the vicinity of the liquidus isotherm for $\theta = \pi$.

Fig. 2 shows a cooling curve identified by numbers associated with energy release during the process of nucleation and phase growth. When the temperature reaches point 1, the nucleation process begins with a temperature decrease to point 2 in relation to the undercooling in the liquid $\Delta T = T_L - T$ because above point 1, nucleation of a new phase cannot take place for a given thermal field $\nabla \mathbf{T}$ because the surface entropy would be infinite for $\Delta T \rightarrow 0$, as seen in Eq. (16a) and Eq. (17a). Considering δ is the piecewise Heaviside function, which depends on the heat flux signal.

$$\delta(\vec{q}) = \begin{cases} 1 \ for \ \vec{q} > 0 \\ 0 \ for \ \vec{q} < 0 \end{cases} \tag{18}$$

10

The energy associated with thermal resistance to nucleation from point 1 to point 2, the barrier to overcome associated with a thermal field $\nabla\mathbf{T}$ and an isothermal velocity $\frac{dA_L}{dt}\ [m^2 s^{-1}]$, is given as follows:

$$(1-\delta)\frac{h_L}{T_L}\frac{\Gamma_L(\vec{r})}{v_L} = (1-\delta)\, S_L \frac{\Gamma_L(\vec{r})}{v_L} \tag{19}$$

Depending on the level of the cooling rate associated with the thermal field gradient $\nabla\mathbf{T}$ normal to the created and deformed surface area $A(\vec{r})$, the temperature may not return to point 3, and therefore, the release of latent heat will be partial below $\Delta H_f < \Delta H$, characterizing a lower state of crystal ordering. A regular monocrystal will present the highest possible state of crystal ordering, as verified by Eq. (16) and Eq. (17), and thus the highest possible release of latent heat, representing the equilibrium state, where no residual deformation would be observed in the crystal. From point 3, or below it due to the local thermal gradient, to point 5, latent heat is released from a $(1-\delta)\frac{\Delta H}{v_L - v_S}$ amount, simultaneously with the advancement of the interface to the next nucleation position, where it will advance due to further coalescence, and the process repeats continuously. If there are conditions adverse to the nucleation process ahead at the transformation interface, the interface advance ceases immediately. Nucleation can be selectively enhanced without increasing the rate of crystal growth, which is achieved by adjusting the thermal field [1] and shown in Fig. (2) by paths $5'$ to $5' = 5''$.
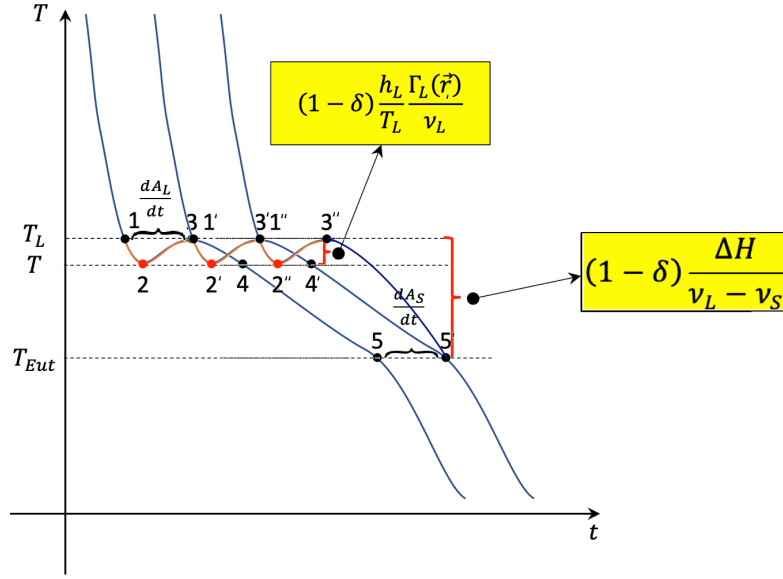
Fig. 2 Schematic representation demonstrating the energies associated with the processes of nucleation and phase growth.

The liquidus transformation interface shown by the solidification scheme in Fig. 2 only represents a solid phase nucleation front, whose velocity is related to the advance to the new position where nucleation will occur. In this case, $\delta = 0$ in the term of energy barrier, i.e., $(1 - \delta)\frac{h_L}{T_L}\frac{\Gamma_L(\vec{r})}{v_L}$ to liquidus evolution in Eq. (17). On the other hand, for a melting process $\delta = 1$, because the liquidus isotherm represents a latent heat absorption front with thermal resistance $\delta\frac{\Delta H}{v_L - v_S}$, and the eutectic interface represents the eutectic nucleation front $\delta\frac{h_S}{T_S}\frac{\Gamma_S(\vec{r}=\vec{s}_S)}{v_S} = \delta S_S \frac{\Gamma_S(\vec{r}=\vec{s}_S)}{v_S}$, as recently demonstrated by Ferreira et al. [19]. A similar pattern can be seen in DTA-DSC for asymmetric heating and cooling cycles [33]. Regarding the direction of heat extraction, associated with melting and cooling, Aniolek and coworkers [34] state that during heating, due to the specific microstructure of the eutectic, where phases are aligned with each other, both phases melt very close to a common temperature on both sides of the eutectic for a high solid fraction. In contrast, upon cooling, you have a liquid that will transform into an alpha phase to later transform into a eutectic; however, near the liquidus isotherm, the liquid fraction

is high. This makes the thermal response distinct for both cases. In the case of Fig. (2), the moving transformation interfaces for liquidus and eutectic are given by

$$\left\{ \delta \frac{\Delta H}{v_L - v_S} + (1 - \delta) \frac{h_L}{T_L} \frac{\Gamma_L(\vec{r} = \vec{S}_L)}{v_L} \right\} \frac{dA_L}{dt} = \left(\vec{k}_{SL} \cdot \nabla \mathbf{T}|_{\vec{r} = \vec{S}_L^-} - \vec{k}_L \cdot \nabla \mathbf{T}|_{\vec{r} = \vec{S}_L^+} \right) \cdot \hat{n}_L \, A_L(\vec{r})$$

(20)

$$\left\{ \delta \frac{h_S}{T_S} \frac{\Gamma_S(\vec{r} = \vec{S}_S)}{v_S} + (1 - \delta) \frac{\Delta H}{v_{SL} - v_S} \right\} \frac{dA_S}{dt} = \left(\vec{k}_S \cdot \nabla \mathbf{T}|_{\vec{r} = \vec{S}_S^-} - \vec{k}_{SL} \cdot \nabla \mathbf{T}|_{\vec{r} = \vec{S}_S^+} \right) \cdot \hat{n}_S \, A_S(\vec{r})$$

(21)

$$\left\{ \delta \frac{h_{EutS}}{T_{Eut}} \frac{\Gamma_{Eut}(\vec{r} = \vec{S}_{Eut})}{v_{EutS}} + (1 - \delta) \frac{\Delta H_{Eut}}{v_S - v_{EutS}} \right\} \frac{dA_{Eut}}{dt} = \left(\vec{k}_{EutS} \cdot \nabla \mathbf{T}|_{\vec{r} = \vec{S}_{EutS}^-} - \vec{k}_{SL} \cdot \nabla \mathbf{T}|_{\vec{r} = \vec{S}_S^+} \right) \cdot \hat{n}_{Eut} \, A_{Eut}(\vec{r})$$

(22)

$$\left\{ (1 - \delta) \frac{h_{SEut}}{T_{Eut}} \frac{\Gamma_{Eut}(\vec{r} = \vec{S}_{Eut})}{v_{SEut}} + \delta \frac{h_{LEut}}{T_{Eut}} \frac{\Gamma_{Eut}(\vec{r} = \vec{S}_{Eut})}{v_{LEut}} + \frac{\Delta H_{Eut}}{v_{EutS} - v_{EutS}} \right\} \frac{dA_{Eut}}{dt} = \left(\vec{k}_{SEut} \cdot \nabla \mathbf{T}|_{\vec{r} = \vec{S}_{SEut}^-} - \vec{k}_{LEut} \cdot \right.$$

$$\left. \nabla \mathbf{T}|_{\vec{r} = \vec{S}_{LEeut}^+} \right) \cdot \hat{n}_{Eut} \, A_{Eut}(\vec{r})$$

(23)

where T_L', T_S' and T_{Eut}' are nonequilibrium temperatures of the isotherms. As previously explained in Fig. 1 for positions 1, 2, and 3, it is worth mentioning due to the portion of surface energy associated with the surface area deformation $A(\varepsilon)\gamma(\varepsilon)$ related to the superficial internal energy, the equilibrium temperatures of isotherms cannot be reached. Therefore, during cooling these temperatures T' will be offset below the equilibrium transformation temperatures or above, in case of heating. Fig. (3) shows a schematic representation of the moving interfaces for solidification/melting referring to a pure component, binary alloy, binary alloy with eutectic reaction and eutectic composition alloy, respectively. The maximum solubility of Cu in FCC_A1 (α-phase) and the eutectic composition are represented by C_{Smax} and C_{Eut}.
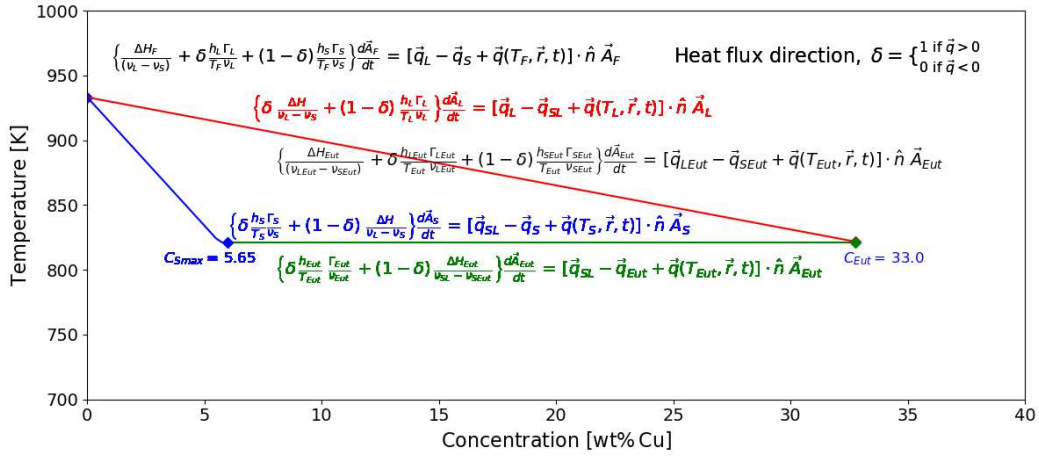
The figure contains a graph with axes Temperature [K] (y-axis, 700 to 1000) and Concentration [wt% Cu] (x-axis, 0 to 40), with overlaid equations:

$$\left\{\frac{\Delta H_F}{(v_L - v_S)} + \delta \frac{h_L \Gamma_L}{T_F v_L} + (1-\delta)\frac{h_S \Gamma_S}{T_F v_S}\right\}\frac{d\vec{A}_F}{dt} = [\vec{q}_L - \vec{q}_S + \vec{q}(T_F, \vec{r}, t)] \cdot \hat{n}\,\vec{A}_F \qquad \text{Heat flux direction, } \delta = \left\{ \begin{matrix} 1 \text{ if } \vec{q} > 0 \\ 0 \text{ if } \vec{q} < 0 \end{matrix} \right.$$

$$\left\{\delta \frac{\Delta H}{v_L - v_S} + (1-\delta)\frac{h_L \Gamma_L}{T_L v_L}\right\}\frac{d\vec{A}_L}{dt} = [\vec{q}_L - \vec{q}_{SL} + \vec{q}(T_L, \vec{r}, t)] \cdot \hat{n}\,\vec{A}_L$$

$$\left\{\frac{\Delta H_{Eut}}{(v_{LEut} - v_{SEut})} + \delta \frac{h_{LEut}\Gamma_{LEut}}{T_{Eut} v_{LEut}} + (1-\delta)\frac{h_{SEut}\Gamma_{SEut}}{T_{Eut}v_{SEut}}\right\}\frac{d\vec{A}_{Eut}}{dt} = [\vec{q}_{LEut} - \vec{q}_{SEut} + \vec{q}(T_{Eut}, \vec{r}, t)] \cdot \hat{n}\,\vec{A}_{Eut}$$

$$\left\{\delta \frac{h_S \Gamma_S}{T_S v_S} + (1-\delta)\frac{\Delta H}{v_L - v_S}\right\}\frac{d\vec{A}_S}{dt} = [\vec{q}_{SL} - \vec{q}_S + \vec{q}(T_S, \vec{r}, t)] \cdot \hat{n}\,\vec{A}_S$$

$C_{Smax} = 5.65$

$$\left\{\delta \frac{h_{Eut}\Gamma_{Eut}}{T_{Eut}v_{Eut}} + (1-\delta)\frac{\Delta H_{Eut}}{v_{SL} - v_{SEut}}\right\}\frac{d\vec{A}_{Eut}}{dt} = [\vec{q}_{SL} - \vec{q}_{Eut} + \vec{q}(T_{Eut}, \vec{r}, t)] \cdot \hat{n}\,\vec{A}_{Eut}$$

$C_{Eut} = 33.0$

Fig. 3 Schematic representation of several solidification moving interfaces.

4. Application of Heterogeneous Nucleation on the Molar Specific Heat Capacity of the Solids

Aiming to validate the effect of the heterogeneous nucleation process on the specific molar capacity of the Al-α phase (FCC_A1) referring to a ternary Al-6wt%Cu-3wt%Si alloy, a brief description of the model of the molar specific heat capacity of solids firstly, derived in 2019 by Ferreira et al. applied to a wide range of pure solid materials [18,35], transition metals [36], phases [37] and ceramics [37,38] will be performed.

$$c_v = \left(1.0 + D_{Comp}(\omega_{Comp})\right) 9 N_a k_B \left(\frac{T}{\Theta_{D,Comp}}\right)^3 \int_0^{\frac{T}{\Theta_{D,Comp}}} \frac{x^4 e^x}{(e^x - 1)^2} dx\, (1 + c_{ve}) + (n + 1/2)\left[9\, c_v^{Rot} + \right.$$

$$\left. \left(1 - \sqrt{\frac{E_i \rho_{Dia}}{E_{Dia}\rho_i}}\right)\frac{RT^3}{\Theta_{D,Comp}\, T_{f,Comp}^2}\right] \qquad (24)$$

The total electronic contribution $c_{ve,i}$ to the electronic molar heat capacity $c_{ve,Comp}$ can be expressed as

$$\sum_{i=1}^{m} x_i \cdot c_{ve,i} \qquad (25)$$

where x_i is the molar fraction of element i. In the case of ceramics, Eq. (25) guarantees the electrical neutrality of the compound.

14

The element i electronic contribution to c_{ve} is written in terms of the phonon energy c_v^{Vib} as follows:

$$\frac{c_{ve,i}}{c_v^{Vib}} = \frac{5}{24\,\pi^3} Z_i \frac{\Theta_{D,i}^3}{T^2\,T_{f,i}^{bulk}} \tag{26}$$

where Z_i is the valence of element i, $T_{f,i}^{bulk}$ is the melting temperature of element i $[K]$ and T is the absolute temperature $[K]$.

The rotational contribution c_v^{Rot} to molar heat capacity was derived by Ferreira et al. [35] and is a quantized contribution of J_i with respect to n,

$$c_v^{Rot} = \frac{5}{4} \frac{R \cdot \hbar^3 \cdot}{k_B^2\,\omega_{D,Comp}(T+\Theta_{D,Comp})^2} \sum_{i=1}^m \frac{x_i \cdot J_i(J_i+1)}{\overline{M}_i \cdot r_i^2} \quad [J.mol^{-1}.K^{-1}] \tag{27}$$

where $\omega_{D,Comp}$ is the maximum admissible frequency known as Debye's frequency.

The magnetic contribution c_v^{mag} to the molar specific heat of solids was deduced by Ferreira et al. [35] as being the quantized value of the ratio of velocities in the solid to that in the diamond, related to the Debye temperature $\Theta_{D,Comp}$, the transformation temperature $T_{f,Comp}$ and the temperature T of the solid.

$$c_v^{mag} = \left(1 - \sqrt{\frac{E_i\,\rho_{Dia}}{E_{Dia}\,\rho_i}}\right) \frac{RT^3}{\Theta_{D,Comp}\,T_{f,Comp}^2} \quad [J.mol^{-1}.K^{-1}] \tag{28}$$

It is worth noting that for very complex dynamic matrices, the ideal solution would be the analytical determination from the potentials of the constituent elements (potential energy density) and the distribution of the mass density along the crystalline directions to compose the map of the constituent elements of the dynamic matrix. In this work, the crystalline moments were considered a one-dimensional projection, as applied previously [39].

The first Brillouin zone is exchanged by an integral over a sphere of radius k_D, containing precisely N wave vectors allowed. As a volume of space k by wave vector, it requires,

$$\frac{(2\pi)^3}{V_C} N = \frac{4\pi k_D^3}{3} \tag{29}$$

Then, the density of atoms n can be obtained as

$$n = \frac{k_D^3}{6\pi^2} = \frac{1}{6\pi^2} \left(\frac{k_B \, \Theta_{D,Comp}}{\hbar \, v}\right)^3 \tag{30}$$

The density of states $D_{Comp}(\omega_{Comp})$ for a compound of critical volume V_C is calculated by the nonequilibrium heterogeneous nucleation model using either the first-order or second-order formulations and the Gibbs-Thomson-Ferreira equation – GTF [18-20],

$$D_{Comp}(\omega_{Comp}) = \frac{V_C \, \omega_{Comp}^2}{2 \, \pi^2 \, v^3} \tag{31}$$

By applying a first-order nonequilibrium nucleation formulation Eq. (16),

$$r_{C,Het} = \frac{2 \, \gamma_{SL}}{\Delta T \left[\left(\Delta S_V - \frac{1}{\Delta T} \frac{\partial \gamma_{SL}}{\partial r}\right) f(\theta) - \frac{\gamma_{SL}}{\Delta T} \frac{\partial f(\theta)}{\partial r}\right]} = \frac{2 \, \Gamma_{Het}}{\Delta T}$$

and

$$\Gamma_{Het} = \frac{\gamma_{SL}}{\left(\Delta S_V - \frac{1}{\Delta T} \frac{\partial \gamma_{SL}}{\partial r}\right) f(\theta) - \frac{\gamma_{SL}}{\Delta T} \frac{\partial f(\theta)}{\partial r}}$$

Finally, the GTF equation Eq. (1) for the coupling of the nucleation process to the thermal field $\nabla \mathbf{T}$,

$$\Gamma_{Het}(\vec{r}) = \nabla \mathbf{T} \cdot \hat{n} \, A(\vec{r}) = \left[\frac{\partial T}{\partial \sigma V} \cdot \nabla \boldsymbol{\sigma} V + \sum_{i=1}^{n-1} \frac{\partial T}{\partial C_i} \cdot \nabla C_i + \nabla T\right]$$

Finally, the critical volume is calculated from the following equation:

$$V_C = \frac{1}{3} \, \pi \, r_{C,Het}^3 \, f(\theta) = \frac{1}{3} \, \pi \, r_{C,Het}^3 \, (2 - 3\cos\theta + \cos^3\theta) \tag{32}$$

5. Results and Discussion

The results and discussion will be divided into four sections: nucleation, nucleating-coalescent transformation moving interface, application of nonequilibrium nucleation to the theoretical determination of the molar specific heat capacity of solids and a simple application for the control of nucleation.

5.1 Nucleation

In this section, the effect of nucleation variables of the Al-α phase (FCC_A1) was calculated as a function of the cooling rate taken near the liquidus and solidus isotherms during transient upward solidification of an Al-based alloy with composition Al-6wt%Cu-3wt%Si. The global heat transfer coefficient $h_g = 4600\ t^{-0.12}\ W.m^{-2}.K^{-1}$ was determined using the IHCP technique [18]. The temperature ∇T and composition gradients ∇C_{Cu} and ∇C_{Si} were calculated numerically, from experimental data by phase change IHCP technique, for a detailed description of the thermal gradient $\nabla \mathbf{T}$, which is necessary to determine the local Gibbs-Thomson coefficient, $\Gamma(\vec{r}) = \nabla \mathbf{T} \cdot \hat{n}\, A(\vec{r}) = \left[\frac{\partial T}{\partial \sigma V} \cdot \nabla \boldsymbol{\sigma} V + \sum_{i=1}^{n-1} \frac{\partial T}{\partial C_i} \cdot \nabla C_i + \nabla T \right] \cdot \hat{n}\, A(\vec{r})$.

Regarding the solution of the critical radius r_C, the Gibbs-Thomson-Ferreira equation - GTF is coupled to one of the nucleation models, either of second-order Eq. (14) or first-order Eq. (16) formulation. In this work, a solution previously developed for the surface-stress tensor for the case of an isotropic medium is employed, considering only the elastic component, associated with the solution proposed for surface energy by Ferreira [18] which considers a spherical metric $\left(r_C/r_{CEq} \right)^2$ and the isotropic surface-stress tensor s, providing $\gamma_{SL} = \frac{\gamma_0}{\left(r_C/r_{CEq} \right)^2} - s$ [38]. The surface tension σ and surface energy γ and their relationship to the surface-stress tensor $s_{i,j} = \delta_{i,j} \gamma + \frac{\partial \gamma}{\partial \varepsilon_{i,j}}$ [40] and the internal surface energy U_{Surf} can be found in [41,42]. For a general thermal gradient $\nabla \mathbf{T}$, this sphere has no constant radius, depending on $\nabla \mathbf{T}$ [18,19], the so-called variable radius sphere, which in the case of nucleation is a simple translation from the spherical space [8,9], expressed as a function of the property Π, $r^2(\Pi) = \sum_{i=1}^{3}\left(x_i - x_{0,i} \right)^2$ and $\Pi = \nabla \mathbf{T}$. For applications in which a given possible nucleating surface shape $A(\vec{r})$ is desired, by controlling the thermal gradient $\nabla \mathbf{T}$, a sphere decoding algorithm [43] is necessary
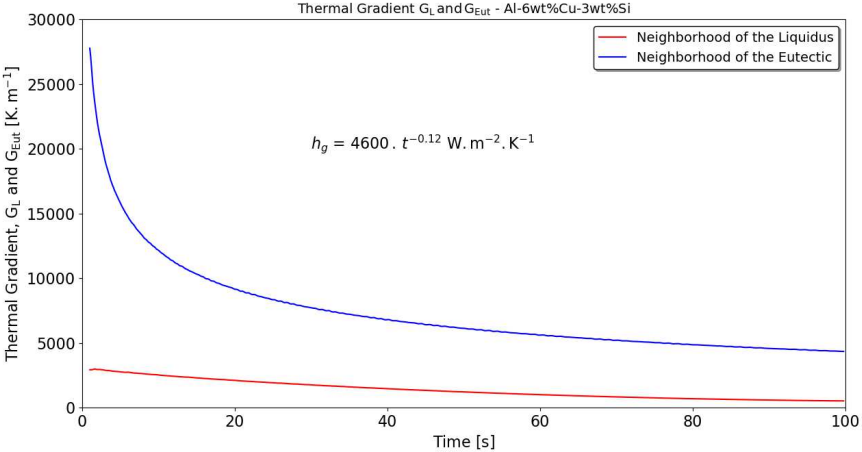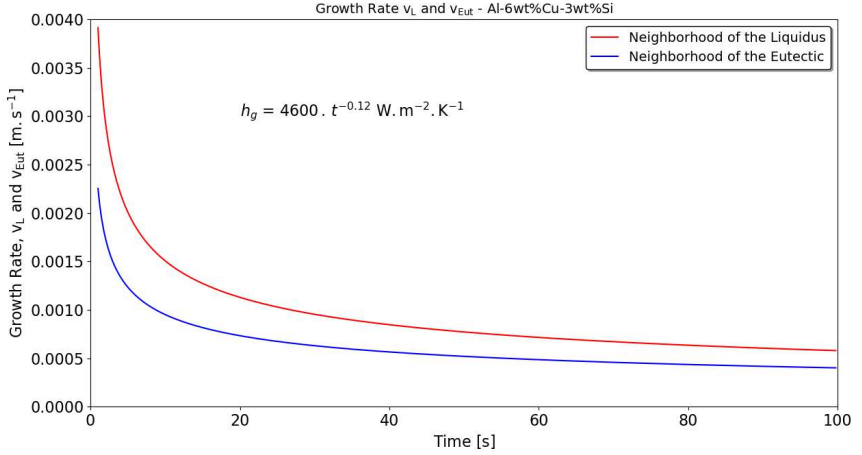
to solve the vector radii unknowns to determine the corresponding thermal gradient $\nabla \mathbf{T}$. The radii are only constant for an isotropic thermal gradient. For the investigated Al-based alloy composition and for the typical maximum cooling rates obtained experimentally, $600 K.min^{-1}$ near the liquidus and $3600 K.min^{-1}$ near the eutectic isotherm, these are considerably low to induce any glass-crystalline transition. Hence, for the present study, the first-order nucleation formulation is suitable,

$$\frac{\frac{\gamma_0}{(r_C/r_{CEq})^2} - s}{\left(\Delta S_V - \frac{1}{\Delta T}\frac{\partial \gamma_{SL}}{\partial r}\right)f(\theta) - \frac{\gamma_{SL}}{\Delta T}\frac{\partial f(\theta)}{\partial r}} = \nabla \mathbf{T} \cdot \hat{n} \, A(\vec{r}_C) = \left[\frac{\partial T}{\partial \sigma V} \cdot \nabla \sigma V + \sum_{i=1}^{n-1}\frac{\partial T}{\partial C_i} \cdot \nabla C_i + \nabla T\right] \cdot \hat{n} \, A(\vec{r}_C) \quad (33)$$

The purpose of analyzing the nucleation variables during the transient solidification process of a ternary alloy is to investigate the effect of the different terms that make up the first- and second-order formulation of the nonequilibrium nucleation as well as the orders of magnitude of the nucleation parameters involved in the actual heat transfer process with phase change. Subsequently, an algorithm to solve a nonequilibrium nucleation model is proposed which is based on the first- and second-order formulations coupled to the Gibbs-Thomson-Ferreira equation [19,20] as well as an auxiliary free energy minimization model.

The Fig. (4) shows the solidification thermal variables whereby the thermal gradients can be expressed in terms of the isotherm velocities and the cooling rates, respectively. In Fig. (4a) the thermal gradients (temperature and concentration gradients) for the liquidus and eutectic isotherms are plotted against time. In the beginning of solidification process, the liquidus and eutectic gradients are about $3000 \, K.m^{-1}$ and $28000 \, K.m^{-1}$, and at final instants around $510 K.m^{-1}$ and $4350 K.m^{-1}$, respectively. The growth rates as a function of time are presented in Fig. (4b). It can be seen that eutectic isotherm velocity is lower than the liquidus as the thermal barrier to be overcome for the liquidus curve to advance is lower than those of completion of α-phase transformation ΔH_α and the fraction of eutectic reaction ΔH_{Eut}. The
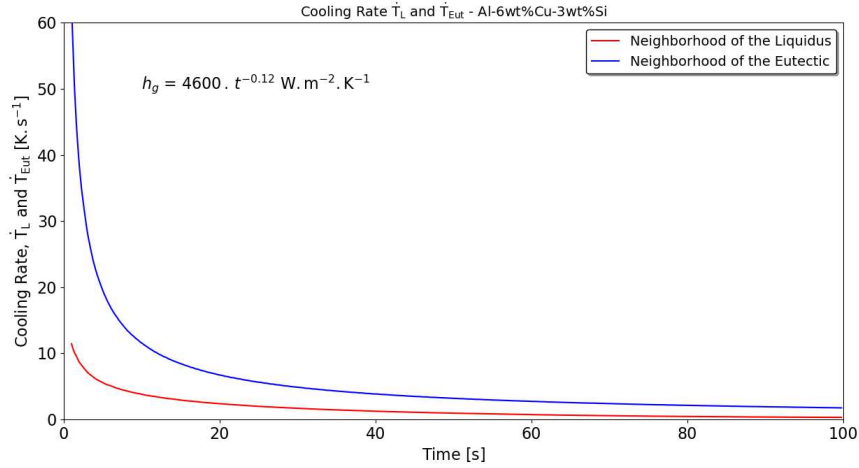
cooling rates in terms of time for the liquidus and eutectic curves shown in Fig. (4c) are obtained

from the correlations between the thermal gradients G_i and the isothermal velocities v_i, given

by $\dot{T}_i = G_i\, v_i$, where $i = L, Eut$.

(a)

(b)

Cooling Rate $\dot{T}_L$ and $\dot{T}_{Eut}$ - Al-6wt%Cu-3wt%Si

$h_g = 4600 . t^{-0.12}$ W.m^{-2}.K^{-1}

(c)

Fig. 4 Transient solidification thermal parameters applied in the evaluation of nucleation variables, (a) thermal gradient, (b) growth rate, and (c) cooling rate.

In Fig. 5, the critical radius r_C is plotted against (a) the liquidus $\dot{T}_L$ and (b) eutectic $\dot{T}_{Eut}$ cooling rates, considering the nucleation angles $\theta = \{\pi, \frac{3\pi}{4}, \frac{\pi}{2}, \frac{\pi}{3}, \frac{\pi}{6}\}$. In Fig. 4(a), the equilibrium critical, r_C for all θ are slightly greater than that of the equilibrium $r_{CEq} \cong$ 4.948μm reckoned by the application of Thermo-calc software and the TTAL7 ThermoTech database at equilibrium. It is also noted that for each θ, the model predicts a value greater or less than the equilibrium for several important nonequilibrium nucleation variables, such as critical radius, surface tension, and surface energy, stating that the equilibrium of these variables is only close to the equilibrium. These values varied considerably with the nucleation angle θ. It is observed for cases (a) and (b) in Fig. 5 that for the same cooling rate, the critical radii are larger for smaller θ, which is an expected behavior. It is observed for cases (a) and (b) in Fig. 5 that for the same cooling rate, the critical radii are larger for smaller θ, which is also an expected. As the cooling rate increase when moving from the liquidus to the eutectic isotherm, one has an intermediate behavior between these limits, thus a progressive decrease in the critical radii. In Fig. 5b, the higher cooling rates cause a considerable decrease in the critical radius in addition to an increase in the ranges for lower θ for low and high rates.
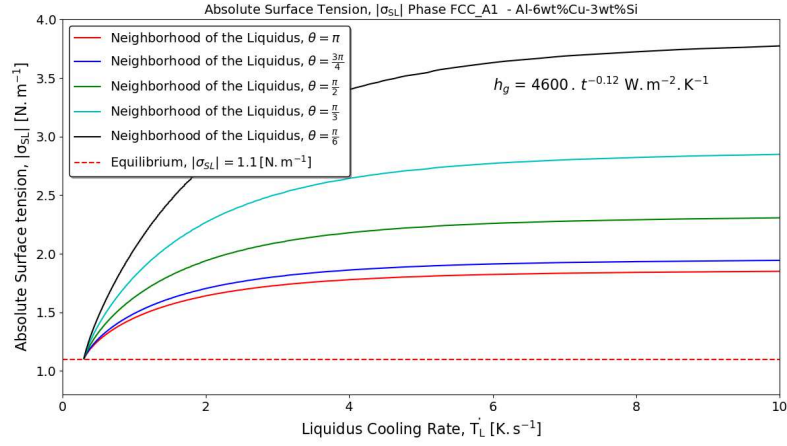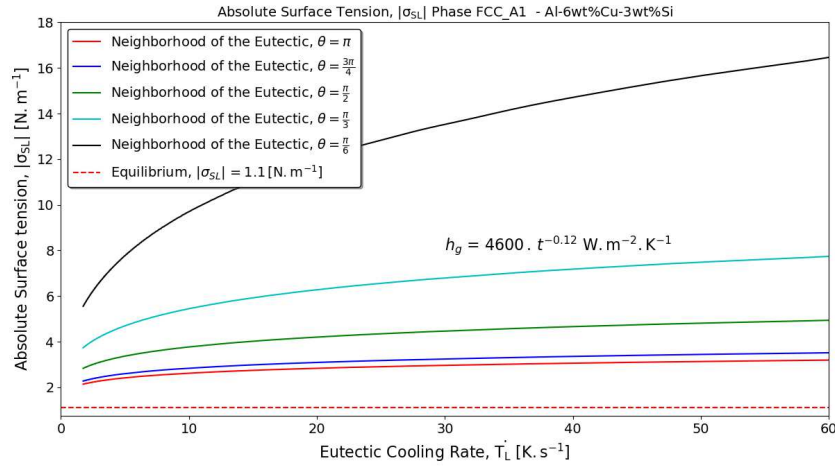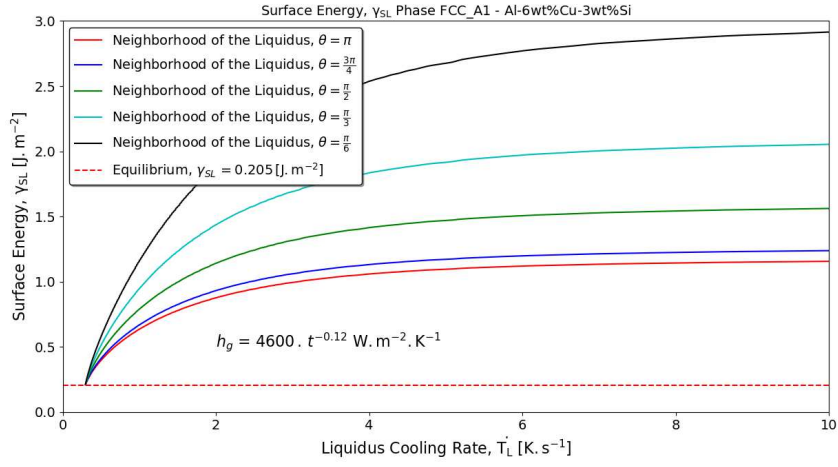
20
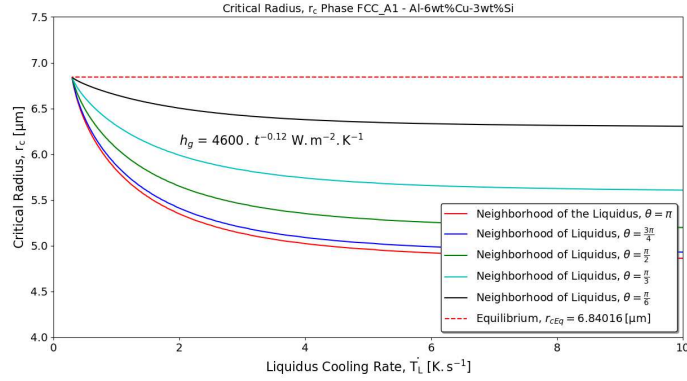
(a)
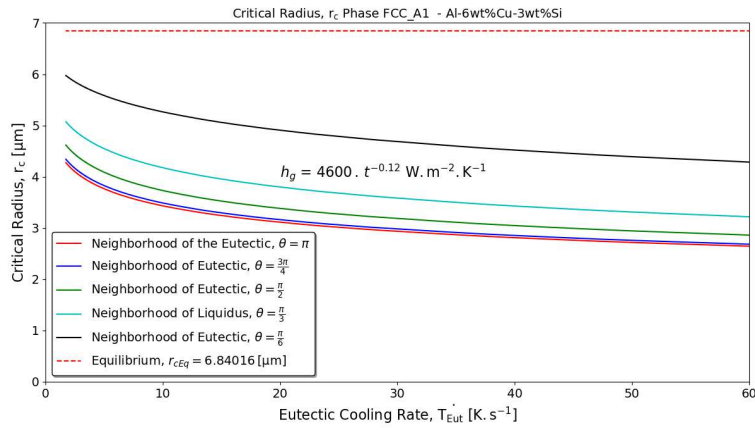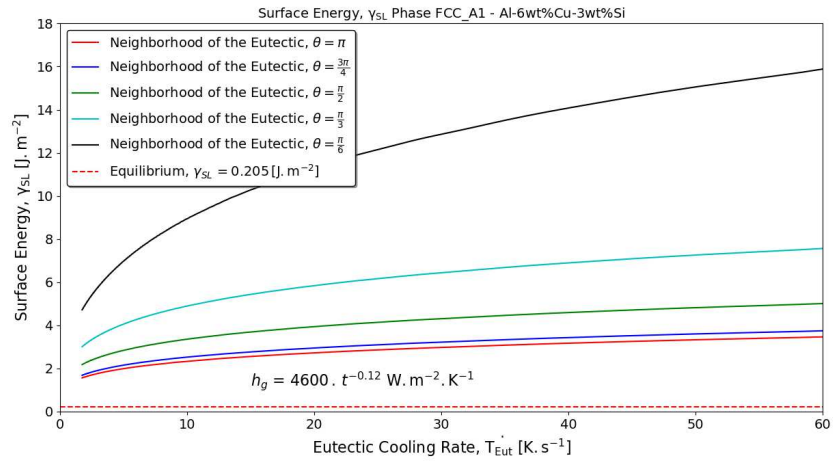

(b)

Fig. 5 Critical radius of non-equilibrium heterogeneous nucleation versus cooling rate, (a) in the neighborhood of the liquidus, and (b) in the neighborhood of the eutectic.

Fig. 6 presents the surface tension modulus expressed in terms of the cooling rate in the vicinity of the (a) liquidus and (b) eutectic isotherms for various nucleation angles θ. In Fig. 6(a), it is observed that for rates very close to zero, the value of the surface tension modulus is close to that presented in the literature for equilibrium $|\sigma| = |\sigma_0|$. However, the same behavior of the simulated curves for r_c was observed, presenting an equilibrium value $|\sigma|$ slightly smaller than $|\sigma_0|$ for all θ. In Fig. 6(b), due to the high cooling rates near the eutectic isotherm, the effect on the solid-liquid stress modulus is quite pronounced, especially for the curves referring to the low nucleation angle θ.
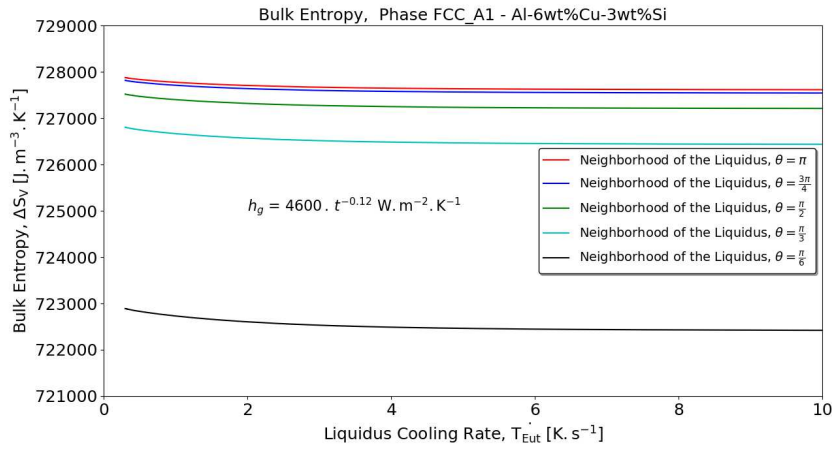
(a)

(b)

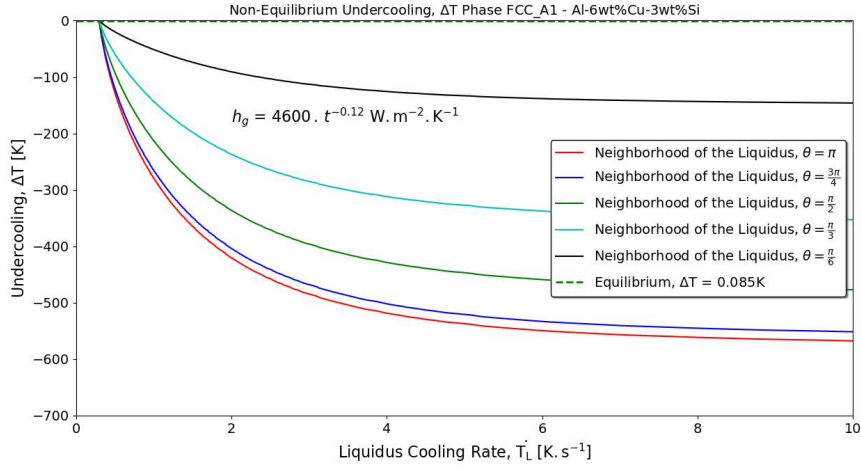Fig. 6 Absolute surface tension of nonequilibrium heterogeneous nucleation against cooling rate, (a) in the neighborhood of the liquidus, and (b) in the neighborhood of the eutectic.

Fig. 7 presents the surface energy γ_{SL} as a function of the nucleation angle θ and the cooling rate in the neighborhood of the (a) liquidus and (b) eutectic isotherms. Fig. 5(a) shows that for low cooling rates, the value of the surface energy is close to that presented in the literature for equilibrium $\gamma_{SL} = \gamma_0$. Similar behavior for surface energy is verified for low cooling rates concerning the equilibrium value γ_0 and curve slope for each nucleation angle θ. In the case of the eutectic cooling rate, the effect on the surface energy is also considerably pronounced for the lowest nucleation angle θ.

(a)

(b)

Fig. 7 Surface energy of non-equilibrium heterogeneous nucleation relative to cooling rate, (a) in the neighborhood of the liquidus, and (b) in the neighborhood of the eutectic.

Fig. 8 presents the nucleation variables expressed in terms of the nucleation angle and the liquidus cooling rate for (a) bulk entropy ΔS_V and (b) undercooling ΔT. By analyzing the bulk entropy variation ΔS_V described in terms of the cooling rate $\dot{T}_L$ and nucleation angle θ, for the case of the smallest θ angles, the highest surface energies γ_{SL} are obtained, as observed in Fig. 7, because the nuclei formed present smaller surface areas in heterogeneous nucleation for $\theta <$

π. When $\dot{T}_L$ increases, the absolute surface tension $|\sigma|$ and the surface energy γ_{SL} increase correspondingly as a consequence of the newly created and deformed surface area $A(\vec{r})$, which causes a decrease in crystalline order, decreasing the bulk entropy ΔS_V in favor of surface entropy ΔS_S. This increase in surface energy γ_{SL} promotes an increase in surface entropy $\Delta S_S = \frac{1}{\Delta T}\frac{\partial \gamma_{SL}}{\partial r}$, promoting a decline in the crystalline order $\Delta S_V < \Delta S_{V\,Eq}$, which implies lower $\Delta H < \Delta H_{Eq}$. In the case of ΔT supercooling, it will be lower for a higher energy contribution from the substrate that will occur for lower values of θ. The smaller the substrate contribution, i.e., for larger angles, $\theta \rightarrow \pi$, the higher the level of supercooling ΔT for a given cooling rate. Fig. 8c presents the undercooling as a function of the cooling rate and the nucleation angle. As stated by several authors [1], the greater the contribution of the substrate during heterogeneous nucleation, i.e., the lower θ, the lower the corresponding level of supercooling ΔT.

(a)

Non-Equilibrium Undercooling, ΔT Phase FCC_A1 - Al-6wt%Cu-3wt%Si

$h_g = 4600 \cdot t^{-0.12}$ W.m^{-2}.K^{-1}

Neighborhood of the Liquidus, $\theta = \pi$
Neighborhood of the Liquidus, $\theta = \frac{3\pi}{4}$
Neighborhood of the Liquidus, $\theta = \frac{\pi}{2}$
Neighborhood of the Liquidus, $\theta = \frac{\pi}{3}$
Neighborhood of the Liquidus, $\theta = \frac{\pi}{6}$
Equilibrium, ΔT = 0.085K

(b)

Fig. 8 Nucleation variables plotted against the cooling rate for (a) bulk entropy, and (b) supercooling.

Fig. 9 presents the nucleation variables expressed in terms of nucleation angle θ and the liquidus cooling rate $\dot{T}_L$ for the derivatives of (a) bulk entropy $\frac{\partial \Delta S_V}{\partial r}$, (b) surface energy $\frac{\partial \gamma_{SL}}{\partial r}$, and (c) supercooling $\frac{\partial \Delta T}{\partial r}$. For the solidification process, $\Delta S_V < 0$, and a positive variation $\frac{\partial \Delta S_V}{\partial r} > 0$ implies a decrease in the bulk entropy $\Delta S_V < \Delta S_{V\,Eq}$ and thus in the crystalline order. In Eq. (14) and Eq. (16), the surface entropy, $\Delta S_S = \frac{1}{\Delta T} \frac{\partial \gamma_{SL}}{\partial r}$ has a negative sign, a positive variation of γ_{SL} in relation to a negative variation of r as the cooling rate $\dot{T}_L$ increases, from which it follows that a negative derivative contributes to an increase in the absolute value of the surface entropy $\Delta S_S > \Delta S_{S\,Eq}$, which depends on the level of stress deforming the nucleated surface area for a given thermal field $\nabla \mathbf{T} \cdot \hat{n}\, A(\vec{r}_C)$. Therefore, a negative derivative of the surface energy $\frac{\partial \gamma_{SL}}{\partial r} < 0$ implies an increase in the surface energy γ_{SL}. Considering the arguments presented, the surface energy increases as the cooling rate increases, as shown in Fig. 7. With respect to the nucleation angle, a low θ substantially impacts the crystalline order, as it contributes to decreasing bulk entropy and increasing surface entropy.
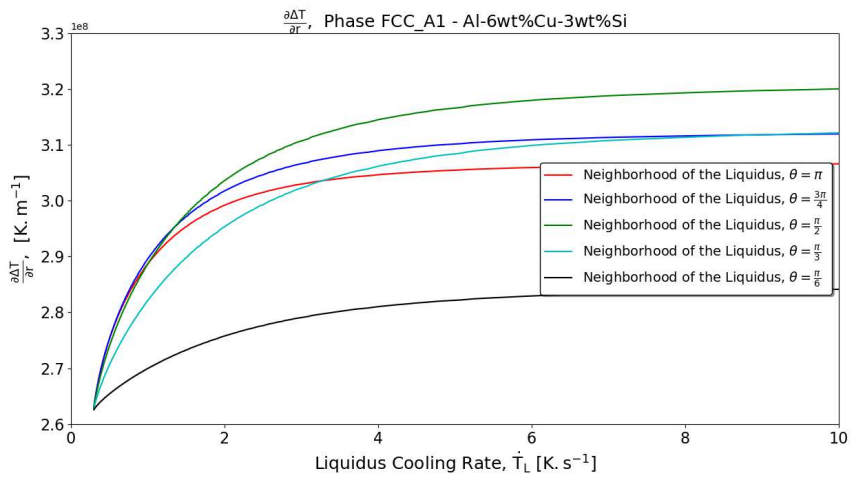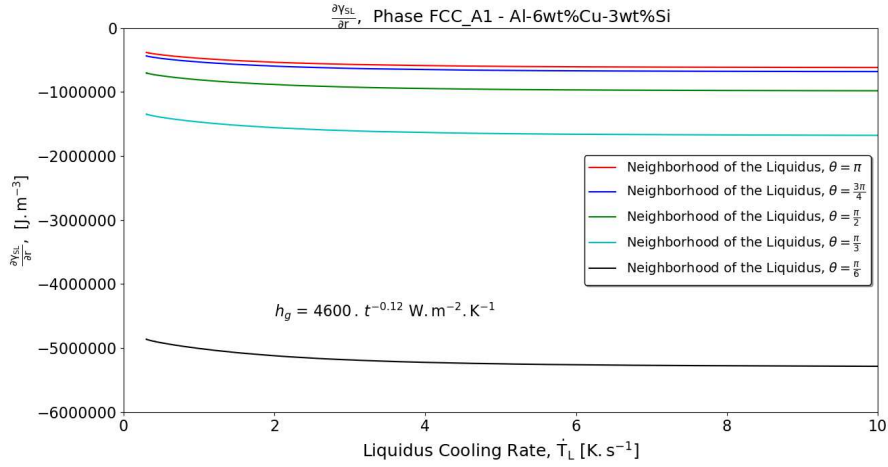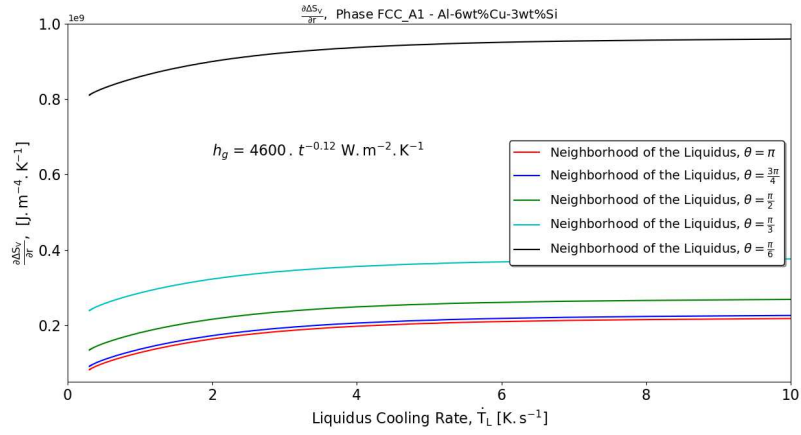
(a)

(b)

(c)

Fig. 9 Nucleation variables plotted against the cooling rate for the derivatives of (a) bulk entropy, (b) surface energy, and (c) supercooling.

Therefore, the simultaneous approach solution for the nucleation critical radius considering a given thermal field requires that the bulk entropy and surface entropy associated with the nucleation angle function $f(\theta) = (2 - 3\cos\theta + \cos^3\theta)$ and the change in the $f(\theta)$ with respect to the critical radius $\frac{\partial f(\theta)}{\partial r}$ can be expressed in terms of the nucleation radius and angle θ:

$$V_\alpha = \frac{\pi}{3}r_C^3 \left(2 - 3\cos\theta + \cos^3\theta\right) \tag{34}$$

By deriving the volume of nucleating phase $V_\alpha = \frac{\pi}{3}r_C^3 \left(2 - 3\cos\theta + \cos^3\theta\right)$ at the equilibrium, the following expression is obtained:

$$dV_\alpha = \frac{\partial V_\alpha}{\partial r_C}dr_C + \frac{\partial V_\alpha}{\partial \theta}d\theta = 0 \tag{35}$$

then,

$$dr_C = -\frac{r_C \sin(\theta)[1+\cos(\theta)]}{2-\cos(\theta)-\cos^2(\theta)}d\theta \tag{36}$$

which provides,

$$\frac{d\theta}{dr_C}r_C = -\frac{2-\cos(\theta)-\cos^2(\theta)}{\sin(\theta)[1+\cos(\theta)]} \tag{37}$$

and,

$$\frac{r_{C\,Het}}{r_{C\,Hom}} = e^{-\int_{\pi}^{\theta} \frac{\sin(\theta)[1+\cos(\theta)]}{2-\cos(\theta)-\cos^2(\theta)} d\theta} \tag{38}$$

By regarding Eq. (35) and Eq. (36), the nucleated α-phase volume $V_\alpha(r_C, \theta)$ can be expressed as follows:

$$f(\theta) + \frac{r_C}{3} \frac{\partial f(\theta)}{\partial r} = -\frac{r_C}{3} \frac{\partial f(\theta)}{\partial \theta} \frac{d\theta}{dr_C} \tag{39}$$

By substituting and simplifying the terms $\frac{\partial f(\theta)}{\partial \theta}$ and $\frac{d\theta}{dr_C}$ into Eq. (39) gives,

$$\frac{\partial f(\theta)}{\partial r} = -3(2 - 3\cos\theta + \cos^3\theta) - [1 - \cos(\theta)][2 - \cos(\theta) - \cos^2(\theta)] \tag{40}$$

Fig. 10 presents (a) $\frac{\partial \theta}{\partial r_C} r_C$, and (b) θ against the nucleation angle θ. As can be seen, the term $\frac{d\theta}{dr_C} r_C$ continuously decreases and becomes $\frac{d\theta}{dr_C} r_C \to -\infty$, as $\theta \to \pi$. On the other hand, Fig. 10 (b), according to Eq. (38), if θ tends to 0 then $\frac{r_{C\,Het}}{r_{C\,Hom}} \to 0$. Otherwise, if $\theta = \pi$, the radii ratio becomes $\frac{r_{C\,Het}}{r_{C\,Hom}} = 1$. The partial and total derivatives of $f(\theta)$ multiplied by r_C are presented in Fig. 10 (c) in which can observed that both curves have a very similar behavior against θ.

(a)

28
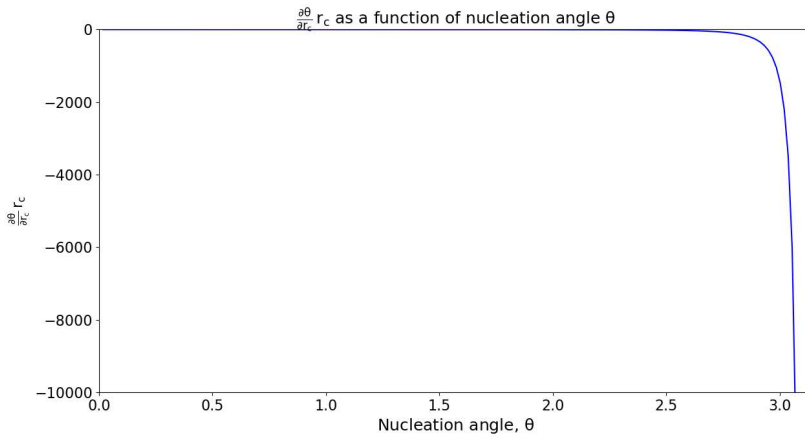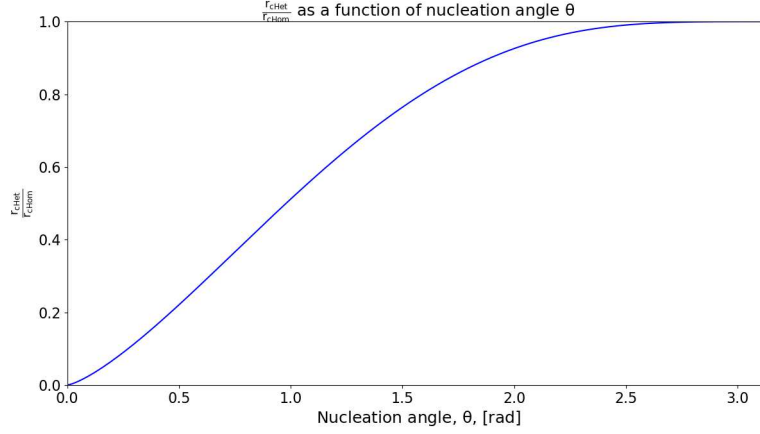
(b)
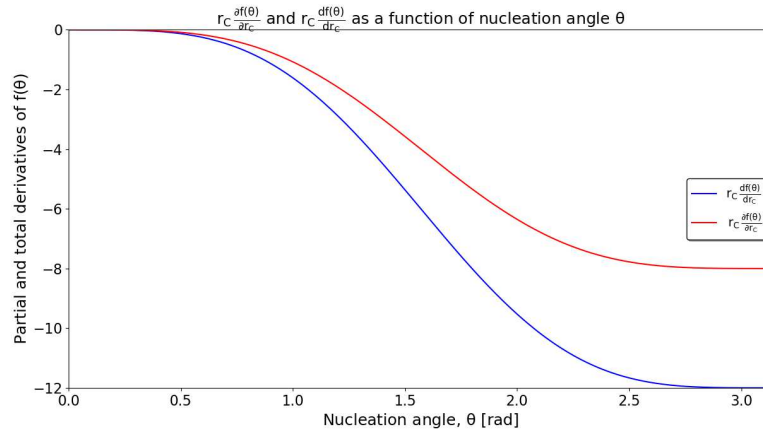
(c)

Fig. 10 Nucleation variables plotted against nucleation angle θ: (a)$r_C \dfrac{\partial \theta}{\partial r_C}$, (b) θ, (c) partial $r_C \dfrac{\partial f(\theta)}{\partial r}$ and total $r_C \dfrac{df(\theta)}{dr}$.

Therefore, the solution of the set of equations for nonequilibrium heterogeneous nucleation can be obtained as follows:

i. For a given thermal field, $\nabla \mathbf{T} \cdot \hat{n} \, A(\vec{r}_C)$ considering a model for the coupling between the surface stress tensor s and the surface energy γ_{SL} [18,19,40-42] Eq.(33);

ii. Then, it is possible to solve simultaneously the equations for second-order nucleation Eq. (10) and Eq. (11) or first-order Eq. (16) and Eq. (17) by evaluating the expressions for s, σ_{SL}, γ_{SL}, θ, $\frac{\partial \theta}{\partial r_C}$, $f(\theta)$, and $\frac{\partial f(\theta)}{\partial r_C}$ as functions of r_C, according to Eq. (35)-Eq.(40);

iii. By applying the set of equations from steps *i* and *ii* at each temperature T below equilibrium, i.e., T_L to map the critical Gibbs free energy for the phases considered to obtain a critical radius $r_{C,Hom}$, $r_{C,Het}$ and supercooling ΔT;

iv. Calculate all other nucleation variables;

v. Repeat the steps *i* to *iv* for each local thermal condition;

5.3 Nucleating-Coalescent Transformation Moving Interface

Starting from a temperature T above T_L, we analyse the heat transfer process associated with the transformation interface that moves along a sample during transient upward solidification. The interface is usually conceptualized as a thermal barrier that must be overcome to move due to thermal field gradients immediately in front of and behind it. Ferreira et al. [19] demonstrated that this thermal barrier is low compared to the level of enthalpy in the liquid for the low thermal gradients in the vicinity of the Liquidus. For a pure metal, nucleation takes place in association with a certain degree of undercooling, the temperature returns to the melting temperature T_f, and the latent heat ΔH_f begins to be released at T_f. Therefore, the following expression is sufficient for the solidification of pure metal and alloys at the eutectic composition:

$$\rho_S \, \Delta H \frac{dS}{dt} = k_S \cdot \left. \frac{\partial \mathrm{T}_S}{\partial \mathrm{z}} \right|_{z=S^-} - k_L \cdot \left. \frac{\partial \mathrm{T}_L}{\partial \mathrm{z}} \right|_{z=S^+} \tag{38}$$

Considering a simple binary alloy, writing an expression for the liquidus and solidus/eutectic interface is impossible since no latent heat is released at the liquidus interface,

and the only possible thermal barrier to interface advance $v_L = \frac{1}{y_0}\frac{dA_L}{dt}$ in this case is the energy

associated with nucleation, $(1-\delta)\frac{h_L}{T_L}\frac{\Gamma_L(\vec{S}_L)}{v_L}$ as $\delta = 1$ for nucleation and displacement dv_L. At

the final instances of the A1-α phase transformation, the latent heat can be integrated as

$(1-\delta)\frac{\Delta H}{v_{SL}-v_S}$ near the eutectic by the final solidus interface. Similarly, for the eutectic, the

amount of heat involved is released at the eutectic temperature T_{Eut} and composition C_{Eut} for

nucleation is $(1-\delta)\frac{h_{SEut}}{T_{Eut}}\frac{\Gamma_{Eut}(\vec{r}=\vec{S}_{Eut})}{v_{SEut}}$, and the latent heat release is given by $\frac{\Delta H_{Eut}}{v_{EutS}-v_{EutS}}$. There

is no other possibility for a liquidus interface in the case of solidification instead of continuous

nucleation and advancement by solid phase coalescence. Recently, Ferreira et al. [19] applied

an analytical model based on the interface formulation for binary alloys, considering the

liquidus cooling rate against the distance from the chill extended here for three levels of

superheating and compared it with Garcia's analytical model for binary alloy transient

solidification, which does not consider any formulation for the liquidus and eutectic interfaces

[44] but rather an energy balance among liquid, solid + liquid and solid phases based on the

thermal gradients. Garcia's model is a closed-form solution for the liquidus interface. As shown

in Fig. 11, the results of both models show good agreement with each other, demonstrating the

existence of a moving nucleating-coalescent interface. In the case of melting, similar behavior

is expected for the eutectic interface, a nucleating-coalescent interface, and latent heat
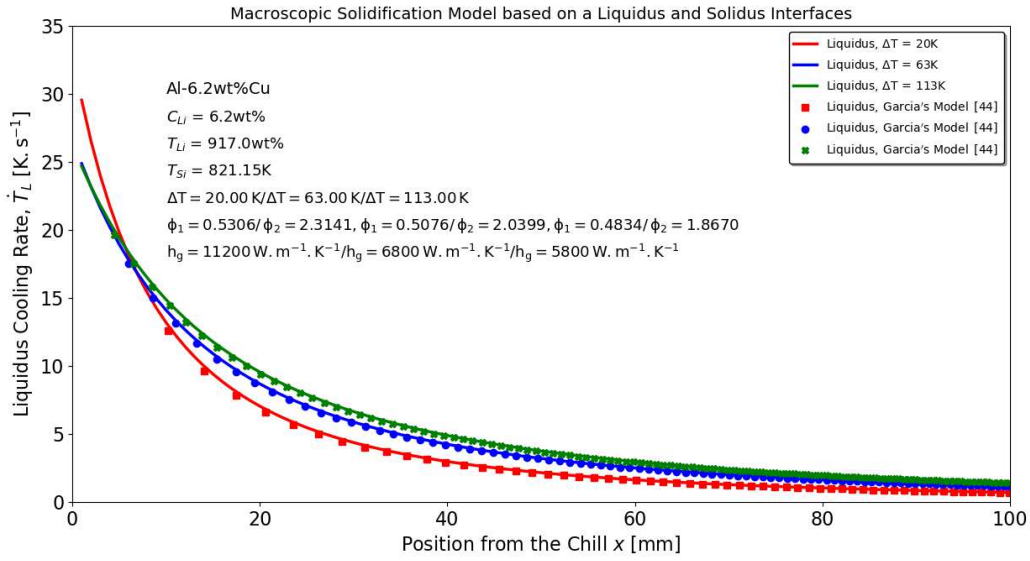
integration at the liquidus.

Fig. 11 Comparison between analytical models considering Al-6.2wt%Cu alloy subjected to different levels of melt superheat liquidus cooling rates concerning the liquidus evolution resistance.

5.3 Application of Non-Equilibrium Nucleation to the Theoretical Determination of the Specific Molar Capacity of Solids

The application of nucleation kinetics to the theoretical model for the specific molar heat capacity of solids is performed for the Al-α phase in a similar way to an experiment employing the differential scanning calorimetry (DSC) technique, although considering a constant cooling rate higher than the limit generally found in DSC experiments. However, it corresponds to the upper limit for the experimental $\dot{T}_L = 10K.s^{-1}$. It is worth noting, that in this set of simulations for evaluation purposes, the theta nucleation angle θ is varied. The results of the theoretical model for the equilibrium condition are compared with those calculated by using Thermo-Calc, exhibiting good agreement. For higher cooling rates, c_P decreases as far as for low θ, as demonstrated in Fig. 12, where $c_P(\pi) > c_P\left(\frac{\pi}{2}\right) > c_P\left(\frac{\pi}{6}\right)$.
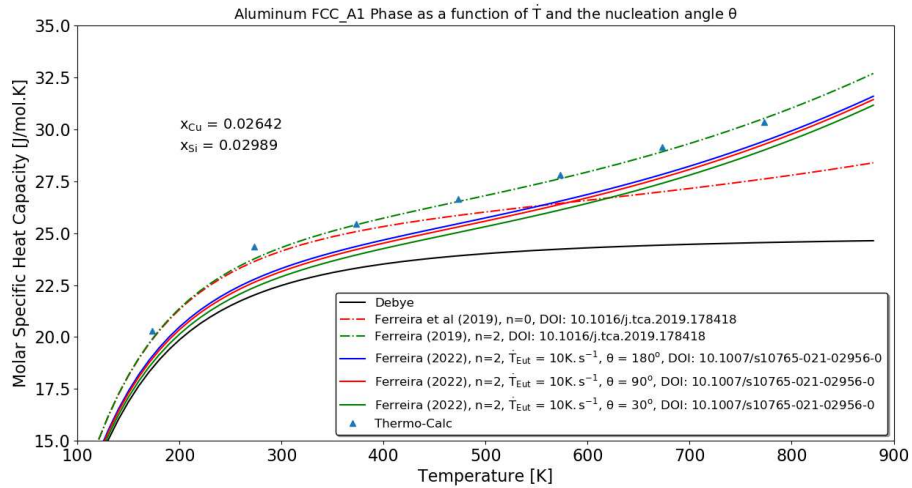
Fig. 12 Comparison of molar heat capacity of FCC_A1 phase against absolute temperature for equilibrium and constant cooling rate for different nucleation angles.

5.4 A Simple Application for the Control of Nucleation

In Fig. 13 the nucleated surface area is divided by a meridian plane that separates two thermal gradient conditions: a region with a constant thermal gradient $\nabla \mathbf{T} = 8938.7 \text{K}.m^{-1}$ and another with a variable thermal gradient according to the equation $\nabla \mathbf{T}(\theta) = 8938.7 + 12835.4 \sin^6(\theta) \text{ K}.m^{-1}$. As can be noted, the anisotropic thermal gradient changed the shape accordingly, demonstrating that the control of nucleus shape is physically possible by the imposition of a known preprogrammed thermal gradient [19,20]. Similar control can be accomplished by nucleant-coalescent moving interface control through a preprogrammed thermal gradient route through the variables of the GTF equation, i.e., temperature, composition, pressure, and volume gradients in an effort to develop a specific shape by precise control of the thermal field variables to achieve a particular desired shape.
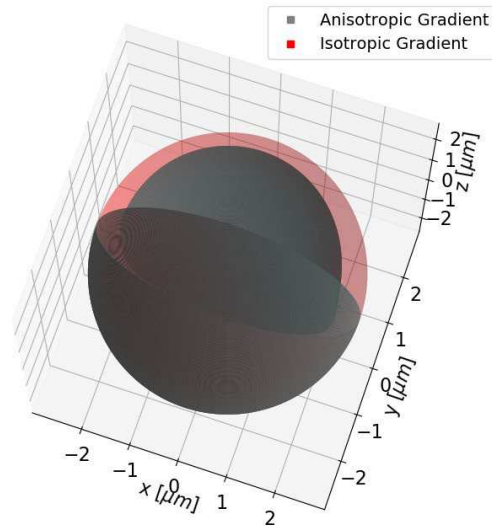
Fig.13 Nucleation of Al-α phase for isotropic and anisotropic thermal gradients separated by a meridian plane.

6. Conclusions

The following major conclusions are derived from the results and discussion held in this paper.

- The derivation of first- and second-order nonequilibrium phase nucleation formulations based on classical thermodynamics and continuous medium is valid for allowing a better understanding of the variables involved in phase nucleation processes, extending the thermodynamic tooling for a better understanding and control of phase change processes in science and technology.

- The second-order formulation is best suited for the study and prediction of nonequilibrium nucleation processes that exhibit glass-crystalline transition.

- Analysis of the variables affecting nonequilibrium nucleation is shown to be physically consistent with the decline in crystal regularity associated with both the increased

cooling rate and the energy contribution of the substrate measured in terms of the low nucleation angles, which is reflected in a decrease in bulk entropy in favor of the surface entropy increasing.

- The existence of a nucleating-coalescing interface was shown to be valid, since in the liquidus isotherm during solidification, or the solidus/eutectic isotherm during fusion, these are only responsible for nucleation and displacement by phase coalescence, once the thermal barrier to be overcome for the advance of these interfaces was determined to be the energy associated with phase nucleating and coalescing. With respect to the other isotherms these are only responsible for the integration of latent heat. These principles allow solutions for nucleation and growth to be deduced analytically [19].

- The lack of an adequate formulation for phase nucleation for the purpose of proper determination of the critical volume for both homogeneous and heterogeneous nonequilibrium nucleation was a major barrier in the theoretical determination of the molar specific heat capacity of solids with respect to the state density, as well as with respect to the glass-crystalline transition. It is worth noting that for a definitive c_p model to be derived, there is a need for the development of theoretical models, especially for those concerning the intermolecular potentials that would allow a ready solution of the dynamic matrix in terms of the distribution of potential energy density and mass density along the directions in complex crystals.

Declarations

Competing interests

The authors declare that they have no known competing financial interests or personal relationships that could have appeared to influence the work reported in this paper.

Authors' contributions

I.L. Ferreira developed the formalism, derived the equations proposed, performed all the computations, and wrote the text. A.L.S. Moreira improved the quality of the text.

Availability of data and materials

The data that support the findings of this study are available from the corresponding author upon reasonable request.

References

1. S. Karthika, T.K. Radhakrishnan, P. Kalaichelvi. Cryst. Growth Des. (2016). https://doi.org/10.1021/acs.cgd.6b00794.

2. W. Kurz, D. J. Fisher. Fundamentals, 4th Ed. Switzerland: Transtech Publications, 1998, **ISBN:** 0878498044.

3. B. Shekunov. Cryst. Growth Des. (2020). https://doi.org/10.1021/acs.cgd.9b00651.

4. Y. Qin, P. Wen, M. Voshage, Y. Chen, P.G. Schückler, L. Jauer, D. Xia, H. Guo, Y. Zheng, J.H. Schleifenbaum. Mater. Des. (2019). https://doi.org/10.1016/j.matdes.2019.107937

5. C. Wei, Z. Zhang, D. Cheng, Z. Sun, M. Zhu, L. Li. Int. J. Extrem. Manuf. (2021). https://doi.org/10.1088/2631-7990/abce04.

6. J. Zhou, Y. Zhou, W. Tang. Crystals (2022). https://doi.org/10.3390/cryst12070980.

7. B. E. Wyslouzil, J. Wölk. J. Chem. Phys. (2016). https://doi.org/10.1063/1.4962283.

8. D. W. Oxtoby, R. Evans. J. Chem. Phys (1988). https://doi.org/10.1063/1.455285.

9. X. C. Zeng, D. W. Oxtoby. J. Chem. Phys. (1991). https://doi.org/10.1063/1.460603.

10. L. Gránásy. J. Non-Cryst. Solids (1993). https://doi.org/10.1016/0022-3093(93)91250-7.

11. L. Gránásy, P. F. James. Proc. R. Soc. London A (1998). https://doi.org/10.1098/rspa.1998.0230.

12. O. Gliko, N. Neumaier, P. Weichun, I. Haase, M. Fisher, A. Bacher, S. Weinkaufm P. G. Vekilov. J. Am. Chem. Soc. (2005). https://doi.org/10.1021/ja043218k.

13. D. V. Alexandrov. Phys. Lett. A (2014). https://doi.org/10.1016/j.physleta.2014.03.051.

14. A. Sauter, F. Roosen-Runge, F. Zhangm G. Lotze, R. M. J. Jacobs, F. Schreiber. J. Am. Chem. Soc. (2015). https://doi.org/10.1021/ja510533x.

15. D. V. Alexandrov, E. V. Makoveeva. Phys. Lett. A (2020). https://doi.org/10.1016/j.physleta.2020.126259.

16. Y. Zhao, D. Song, H. Wang, X. Li, L. Chen, Z. Sun, Z. Wang, T. Zhai, Y. Fu, Y. Wang, S. Liu, Y. Du, W. Zhang. Intermetallics (2022). https://doi.org/10.1016/j.intermet.2022.107584.

17. S. Yang, Z. Guo, B. Bian, J. Du, Y. Hu. J. Phys. Chem. Lett. (2022). https://doi.org/10.1021/acs.jpclett.2c00855.

18. I.L. Ferreira. Int. J. Thermophys. (2022). https://doi.org/10.1007/s10765-021-02956-0.

19. I.L. Ferreira, A. Garcia, A.L.S. Moreira. Int. J. Thermophys. (2022). https://doi.org/10.1007/s10765-022-03099-6.

20. I.L. Ferreira, A.L.S. Moreira, Designing Shape of Nucleus and Grain Coalescence during Alloy Solidification in 3d-ICOMAS Conference. Verona (2022).

21. I. L. Ferreira, A. L. S. Moreira, J. Aviz, T. A. Costa, O. F. L. Rocha, A. S. Barros, A. Garcia. J. Manuf. Proc. (2018). https://doi.org/10.1016/j.jmapro.2018.08.010.

22. I. L. Ferreira, J. A. de Castro, A. Garcia. (2019) In: Wettability and Interfacial Phenomena—Implications for Material Processing. 1ed. London: IntechOpen. https://doi.org/10.5772/intechopen.82307.

23. I. L. Ferreira, A. Garcia. Continuum Mech. Thermodyn. (2020). https://doi.org/10.1007/s00161-019-00836-5.

24. G. Kaptay. Z. Met.kd. (2005). https://doi.org/10.3139/146.018080.

25. I. Egry. Scripta Metall. Mater. (1993). https://doi.org/10.1016/0956-716X(93)90467-7.

26. S. Seetharaman, S. C. Du. Metall. Mater. Trans. B (1994). https://doi.org/10.1007/BF02650079.

27. W. Kurz, M. Rappaz, R. Trivedi. Int. J. Mater. Rev. (2021). https://doi.org/10.1080/09506608.2020.1757894.

28. M. Rappaz, W. J. Boettinger. Acta. Mater. (1999). https://doi.org/10.1016/S1359-6454(99)001880-3.

29. V. Kapil, C. Schran, A. Zen, J. Chen, C.J. Pickard, A. Michaelides. Nature (2022). https://doi.org/10.1038/s41586-022-05036-x.

30. K. Libbrecht. American Scientist (2007). https://doi.org/10.1511/2007.63.52.

31. N. T. H. Oanh, D. N. Binh, D. D. Duc, Q. H. T. Ngoc, N. H. Viet. Materials (2021). https://doi.org/10.3390/ma14143978.

32. J. Pijuan, S. A. Cegarra, S. Dista, V. Albaladejo-Fuentes, M. D. Riera. Materials (2022). https://doi.org/10.3390/ma15228159.

33. K. Kus, T. Breczko. Mater. Phys. Mech. (2010). https://doi.org/10.1088/2053-1591/ab3e95

34. M. Aniolek, T. Smith, F. Czerwinski. Metals (2021). https://doi.org/10.3390/met11020372.

35. I. L. Ferreira, J. A. de Castro, A. Garcia. Thermochim. Acta (2019). https://doi.org/10.1016/j.tca.2019.178418.

36. I. L. Ferreira, J. A. Castro, A. Garcia. In book: Recent advances on numerical simulation. INTECHOPEN: London (2021). https://doi.org/10.5772/intechopen.96880.

37. I. L. Ferreira. Mater. Res. (2021). https://doi.org/10.1590/1980-5373-MR-2020-0529.

38. I.L. Ferreira. Int. J. Thermophys. (2021). https://doi.org/10.1007/s10765-021-02903-z.

39. S. H. Simon. The Oxford Solid State Basics. 1 Ed. Oxford University Press: United Kingdom (2013), ISBN: 978-0-19-968076-4.

40. R. Shuttleworth. Proc. Phys. Soc. A (1950). https://doi.org/10.1088/0370-1298/63/5/302.

41. P. Müller, A. Saul. Surf. Sci. Rep. (2004). https://doi.org/10.1016/j.surfrep.2004.05.001.

42. P. Müller, A. Saul, F. Leroy. Nanosci. Nanotechnol. (2014). https://doi.org/10.1088/2043-6262/5/1/013002.

43. W. Di, L. Dezhi, W. Zhenyong. Comp. Sci. Info. Technol. (2015). https://doi.org/10.5121/csit.2015.51104.

44. J.M.V. Quaresma, C.A. Santos, A. Garcia, Metall. Mater. Trans. A: Phys. Metall. Mater. Sci. (2000). https://doi.org/10.1007/s11661-000-0096-0.